

Structural, electrical and magneto-electric characteristics of complex multiferroic perovskite $\text{Bi}_{0.5}\text{Pb}_{0.5}\text{Fe}_{0.5}\text{Ce}_{0.5}\text{O}_3$

Kalpana Parida¹ · Sujit Kumar Dehury²  · R. N. P. Choudhary¹

Received: 22 February 2016 / Accepted: 21 June 2016 / Published online: 28 June 2016
© Springer Science+Business Media New York 2016

Abstract The polycrystalline sample of bismuth based-complex multiferroic of a composition $\text{Bi}_{0.5}\text{Pb}_{0.5}\text{Fe}_{0.5}\text{Ce}_{0.5}\text{O}_3$ was prepared by a high-temperature solid-state reaction technique (calcinations temperature = 900 °C, sintering temperature = 960 °C, time = 4 h). Preliminary structural analysis using XRD data exhibits the formation of a single-phase compound. Studies of surface morphology of the ceramic sample of the compound, recorded at room temperature using a scanning electron microscope, show uniform distribution of grains of different size with few voids. Detailed studies of dielectric properties (ϵ_r , $\tan \delta$) supported the existence of multiferroic properties in the above complex system. The analysis of impedance parameters, recorded in a wide frequency (1 kHz–1 MHz) and temperature (room temperature to 450 °C) range of the material provide better understanding of (a) role of grains and grain boundaries in resistive and capacitive characteristics, (c) structure-properties relationship and (b) type of relaxation process occurred in the material. Study of temperature dependence of dc conductivity of the compound shows the existence of negative temperature coefficient of resistance in it. The nature of variation of ac conductivity with temperature of the material follows the Jsher's universal power law. Study of magneto-electric characteristics of the sample at room temperature has provided many useful and new data on magneto-electric coupling coefficient of different orders.

1 Introduction

Now-a-days, some materials with the simultaneous existence of opposite nature and phenomenon (i.e., ferroelectric and ferromagnetic) in a single phase (known as multiferroics) are found to be useful for multifunctional devices. Recently, multiferroism (coupling between charge and spin in distorted system) is observed in bismuth ferrite (BiFeO_3) at room temperature ($T_c = 1100$ K, $T_N = 650$ K) [1–3]. Unfortunately, this material has many inherent problems including large leakage current [4, 5], formation of multiphase, unstable structure [6, 7], etc. Which limit the material to be used for meaningful devices. Several attempts have been made to solve these problems such as substitution of suitable element (s) at different atomic site of bismuth ferrite, formation of its solid solution and/or composite with other compounds. During last decade, multiferroic properties including coupling coefficient of bismuth ferrite have been modified or enhanced by substituting rare-earth elements at the Bi-site [8], Co/Mn at the Fe-site [9] and/or fabricating composites with other ferroelectric and ferro/antiferromagnetic oxides of different structures [10]. For further improvement of the quality of the bismuth ferrite for multifunctional applications, we are still in search of new materials of different structural family and properties. As fabrication and detailed studies of bismuth ferrite solid solution or complexes with ACeO_3 perovskites ($A = \text{Pb}$, alkaline earth metals) have not been attempted, structural, electrical, magnetic and magneto-electric properties of complex bismuth ferrite with these cerium compounds have been studied in different experimental conditions. The alkaline earth metals and lead-based cerium compounds have either distorted perovskite or orthorhombic structure with multiple interesting properties. As it is

✉ Sujit Kumar Dehury
sujitam@rediffmail.com

¹ Department of Physics, Siksha 'O' Anusandhan University, Khandagiri Square, Bhubaneswar, India

² Department of Chemistry, Siksha 'O' Anusandhan University, Khandagiri Square, Bhubaneswar 751030, India

expected to solve some inherent problems of bismuth ferrite with enhancement/modification of multiferroic (ferroelectric/ferromagnetic) properties, we have fabricated solid solution or bismuth-based complex multiferroic, first with PbCeO_3 in equal ratio ($\text{Bi}_{0.5}\text{Pb}_{0.5}\text{Fe}_{0.5}\text{Ce}_{0.5}\text{O}_3$). It is expected that this ratio may modify the multiferroic properties significantly. In this paper, we report structural, electrical and magneto-electric properties of the said composition of two independent perovskite systems.

2 Experimental

The high-temperature solid-state reaction method was used to fabricate the polycrystalline (ceramic) sample of complex bismuth ferrite multiferroic ($\text{Bi}_{0.5}\text{Pb}_{0.5}\text{Fe}_{0.5}\text{Ce}_{0.5}\text{O}_3$) using high-purity (AR grade) ingredients: lead oxide (PbO) (M/s Loba Chemie Co.), cerium oxide (CeO_2) (M/s Loba Chemie Co.), bismuth oxide (Bi_2O_3) and iron oxide (Fe_2O_3). The stoichiometric amount of these raw materials was mixed thoroughly in an agate mortar for 2 h in air as well as in methanol. The mixture was repeatedly heated at different temperature, and then finely calcined at $900\text{ }^\circ\text{C}$ for 4 h in a high-purity alumina crucible. The formation of the compound was checked using room temperature X-ray diffraction (XRD) pattern recorded by X-ray powder diffractometer (model D8 Advance of M/s Bruker Co) with $\text{CuK}\alpha$ radiation (wavelength = 1.5405 \AA) on calcined powder in a wide range of Bragg angles ($20^\circ \leq 2\theta \leq 80^\circ$). The calcined powder of the confirmed compound was pressed into pellets (10 mm diameter and 1–2 mm thickness) and sintered at $960\text{ }^\circ\text{C}$ in air for 12 h followed by furnace cooling. The morphology (microstructure) of the sintered pellet was obtained by a scanning electron microscope (SEM), which revealed the formation of high-density pellet sample (with few voids only). For electrical characterization, a thin layer of highly conducting silver paint was coated on both sides of the sintered sample, followed by heat treatment at $150\text{ }^\circ\text{C}$ for 45 min to remove the moisture, if any. An impedance analyzer (phase sensitive meter, PSM) was used to measure dielectric, impedance and related parameters in a wide frequency (1 kHz–1 MHz) range at different temperatures (room temperature to $450\text{ }^\circ\text{C}$). The magneto-electric (ME) set up (M/s Marine India) connected to lock in amplifier (SR 830) was used to measure and calculate the ME coupling coefficients. A Helmholtz coil (200 turns and radius = 2.5 cm) produced the AC magnetic field whereas the DC magnetic field was generated by an electromagnet (maximum field up to 7 kOe). The sample was placed longitudinally in the set up, and the voltage developed across the sample was measured.

3 Results and discussion

3.1 Structural and micro structural studies

Figure 1a shows the room-temperature XRD pattern of the $\text{Bi}_{0.5}\text{Pb}_{0.5}\text{Fe}_{0.5}\text{Ce}_{0.5}\text{O}_3$ (BPFCEO) calcined powder. There are a number of peaks in the XRD pattern, which are different from those of the ingredients, and thus confirming the formation of a new polycrystalline single-phase compound. Preliminary structural analysis was carried out using all the diffraction peaks in a standard computer program package ‘POWD’ [11]. For this analysis, most of the diffraction peaks of the compound were indexed in different crystal systems and unit cell configurations. Based on the best agreement between observed and calculated inter-planar spacing (d), monoclinic crystal system and an unit cell were finally selected. The lattice parameters of the selected unit cell were refined using the least-squares subroutine of the standard computer program package (POWD). The refined lattice parameters are: $a = 3.922(3)\text{ \AA}$, $b = 8.640(3)\text{ \AA}$, $c = 31.128(3)\text{ \AA}$ and $\beta = 92.38$ (figure in the parenthesis of lattice parameters indicates the estimated standard deviation).

The crystallite size (p) of the sample was calculated using the full peak width at half maximum of some distinct peaks (widely spread) in the Scherrer’s relation [12], $p = k\lambda/\beta_{1/2} \cos \theta$ ($k = \text{constant} = 0.89$, $\lambda = 0.15418\text{ nm}$), where $\beta_{1/2}$ is the peak width at half maximum and θ is the peak position. The average crystallite size is found out to be about 46 nm. For the calculation of p , the broadening due to strain, instruments and other effects was ignored since powder sample was used to record XRD profile.

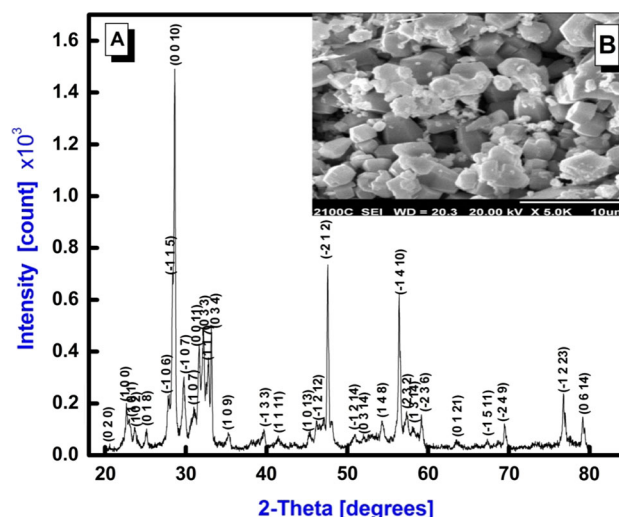


Fig. 1 XRD pattern (a) and typical SEM micrograph (b) of $\text{Bi}_{0.5}\text{Pb}_{0.5}\text{Fe}_{0.5}\text{Ce}_{0.5}\text{O}_3$

The room temperature SEM micrograph of a pellet sample is shown in Fig. 1 (inset, B). It is observed that some small grains of almost equal dimensions but different shapes are uniformly distributed over the entire surface of the sample. The different shapes and size of grains of microstructure indicate the polycrystalline nature of the sample. In spite of sintering at optimized high temperature, some voids of irregular dimension (shape and size) are still observed. The grain size is found to be in the range of 2–7 μm .

3.2 Dielectric properties

Figure 2 shows the frequency dependence of relative dielectric constant (ϵ_r) and tangent loss ($\tan \delta$) of $\text{Bi}_{0.5}\text{Pb}_{0.5}\text{Fe}_{0.5}\text{Ce}_{0.5}\text{O}_3$ in the frequency range of 1 kHz–1 MHz at different temperatures (25–400 °C). As shown in the figure, the relative dielectric constant (ϵ_r) is very high in the low-frequency region which gradually decreases with increase in frequency. Thus, the low-frequency region shows dispersion. At low frequencies, different types of polarizations (i.e., dipolar, interfacial, ionic, atomic and electronic) contribute to the dielectric constant. As the frequency increases beyond a certain limit, dipoles are not able to align themselves with the applied electric field and contribution from different polarizations (except electronic) ceases. Only electronic polarization has a significant contribution to the dielectric constant at higher frequencies, and subsequently the dielectric constant becomes invariant. The loss tangent also decreases in the same manner as of dielectric constant, which can be explained by a two-layer model of Maxwell and Wagner which is based on Koop’s phenomenological theory [13, 14]. According to this

model, the dielectric structure of ceramic material is made of from two layers (i.e., the conducting grains and poorly conducting grain boundaries). In electrical conduction, electrons are more active at grain boundaries in the low-frequency region, and at grains in the high-frequency region. As the grain boundaries are having high resistance, more energy is required for motion of charge carriers in the low-frequency region. Thus, the tangent loss ($\tan \delta$) is also high in this region. The less energy is required for the motion of charge carriers in the high-frequency region due to low resistance, consequently dielectric loss is low.

Figure 3 shows the variation of relative dielectric constant (ϵ_r) and loss tangent as a function of temperature at some selected frequencies of $\text{Bi}_{0.5}\text{Pb}_{0.5}\text{Fe}_{0.5}\text{Ce}_{0.5}\text{O}_3$.

It was observed from the plot that the value of dielectric constant is almost constant in the low- and medium-temperature ranges, and then increases gradually on increasing temperature. It is constant up to 250 °C, and above this temperature, it exhibits a sharp increase up to 350 °C. The value of dielectric constant is found to be within a range of 20–140 k for the frequency range of 1 kHz–1 MHz. The tangent loss factor also shows an almost constant value up to 220 °C, and then, it increases with the rise in temperature. The value of room-temperature $\tan \delta$ is very small (~ 0.004) in the low-temperature region which suggests that $\text{Bi}_{0.5}\text{Pb}_{0.5}\text{Fe}_{0.5}\text{Ce}_{0.5}\text{O}_3$ is suitable for some device applications. The sharp increase in the above parameters may be due to scattering of thermally activated charge carriers or may be due to some defects in the sample [15]. As the ferroelectric-paraelectric transition temperature of $\text{Bi}_{0.5}\text{Pb}_{0.5}\text{Fe}_{0.5}\text{Ce}_{0.5}\text{O}_3$ is expected to be well above the studied temperature region because of the very high transition temperature of BFO, we could not observe any anomaly in the dielectric constant versus temperature curve in our experimental study. However, a small dielectric anomaly observed above 300 °C may be related to the magnetic transition (Neel temperature) as observed in BiFeO_3 .

3.3 Impedance spectral analysis

Figure 4 (left) shows frequency dependence of real part of impedance (Z') at some selected temperatures. The value of Z' decreases with rise in both frequency and temperature, which indicates an increase in its conductivity. The decrease in the magnitude of Z' with increase in temperature in the low-frequency region shows the negative temperature coefficient of resistance (NTCR) behaviour of the material. A merger of curves at high frequencies is due to the possible release of space charge [16]. As a result, the lowering of the barrier properties of the materials at higher temperatures in the high-frequency region is observed. Figure 4 (right) represents the variation of the imaginary

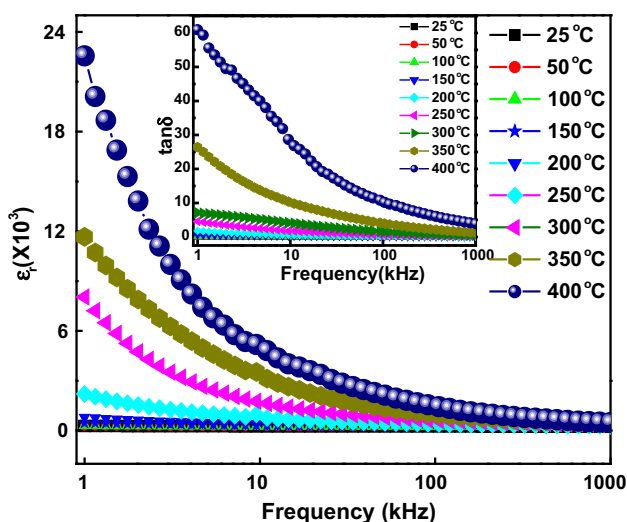


Fig. 2 Frequency dependence of (ϵ_r) and $\tan \delta$ of $\text{Bi}_{0.5}\text{Pb}_{0.5}\text{Fe}_{0.5}\text{Ce}_{0.5}\text{O}_3$ at different temperatures

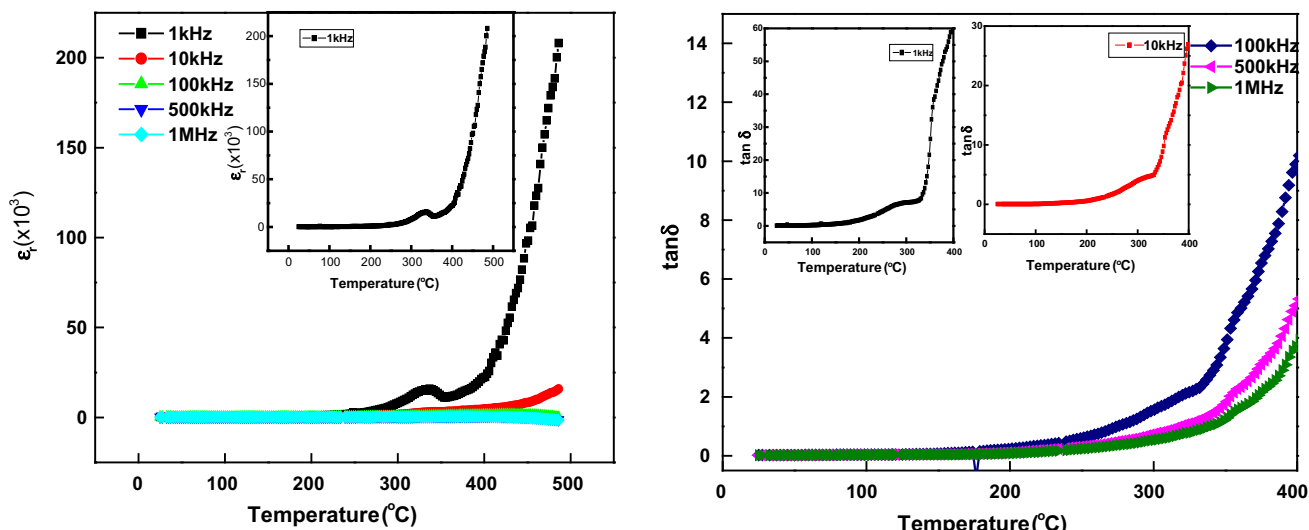


Fig. 3 Temperature dependence of (ϵ_r) (left) and $\tan\delta$ (right) of $\text{Bi}_{0.5}\text{Pb}_{0.5}\text{Fe}_{0.5}\text{Ce}_{0.5}\text{O}_3$

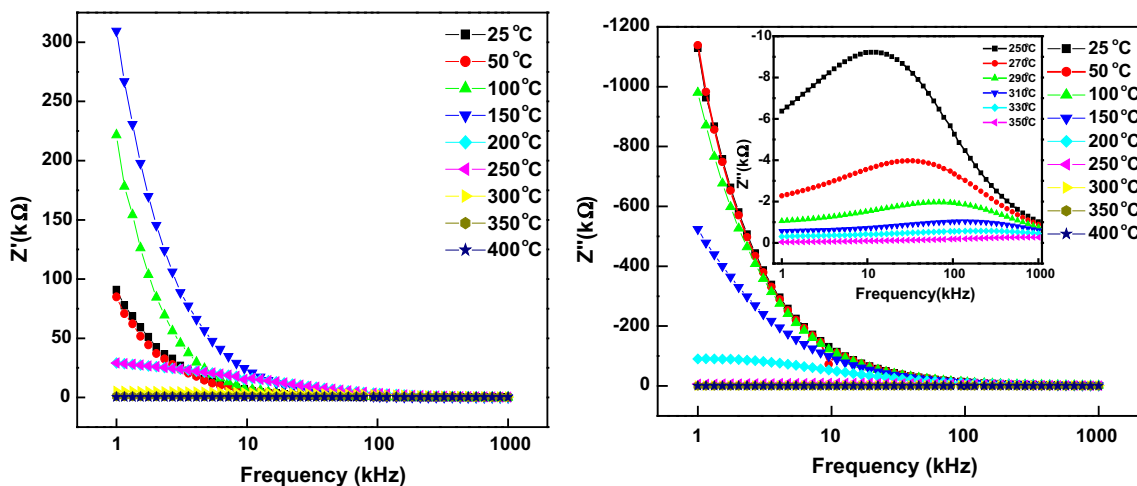


Fig. 4 Variation of Z' (left) and Z'' (right) with frequency at some selected temperatures of $\text{Bi}_{0.5}\text{Pb}_{0.5}\text{Fe}_{0.5}\text{Ce}_{0.5}\text{O}_3$

(Z'') part of the impedance with frequency of $\text{Bi}_{0.5}\text{Pb}_{0.5}\text{Fe}_{0.5}\text{Ce}_{0.5}\text{O}_3$ at different temperatures. It is observed that peaks with asymmetric broadening shift toward the high-frequency side with rise in temperature. It has also observed that the spectra merge at high frequencies irrespective of the temperature. These results suggest the presence of electrical relaxation process in the material, which is temperature dependence of relaxation time [13, 17]. Also, asymmetric broadening of the peak with rise in temperature indicates existence of multiple relaxation times. The relaxation species may possibly be electrons/immobile charges at low temperature and oxygen vacancies/defects at higher temperatures. The electrical conduction in the material arises only by hopping of electron/oxygen ion vacancies among the available localized sites.

The impedance data taken over a wide frequencies range at various temperatures as a Nyquist diagram (complex

impedance spectrum) are presented in Fig. 5. The semi-circular arcs, appeared in the Nyquist plots, can be assigned to the grain interior, grain boundary and/or material–interface electrode effects. These effects are normally explained by an equivalent circuits built up by parallel resistances and capacitances connected in series and an individual RC network being responsible for a single semicircle. Ideal semicircular arcs with its centre on the real Z axis are generally obtained for Debye type relaxation. But due to imperfections in most of the solids, we obtain depressed semicircles (centre below the real Z axis) at high temperatures which show non-Debye type of relaxation mechanism. The departure from the Debye type relaxation can be represented by including a constant phase element (CPE) with the parallel RC network. It suggests the departure from ideal Debye behavior and justifies the presence of a CPE [16] in fitting of the circuit. The CPE

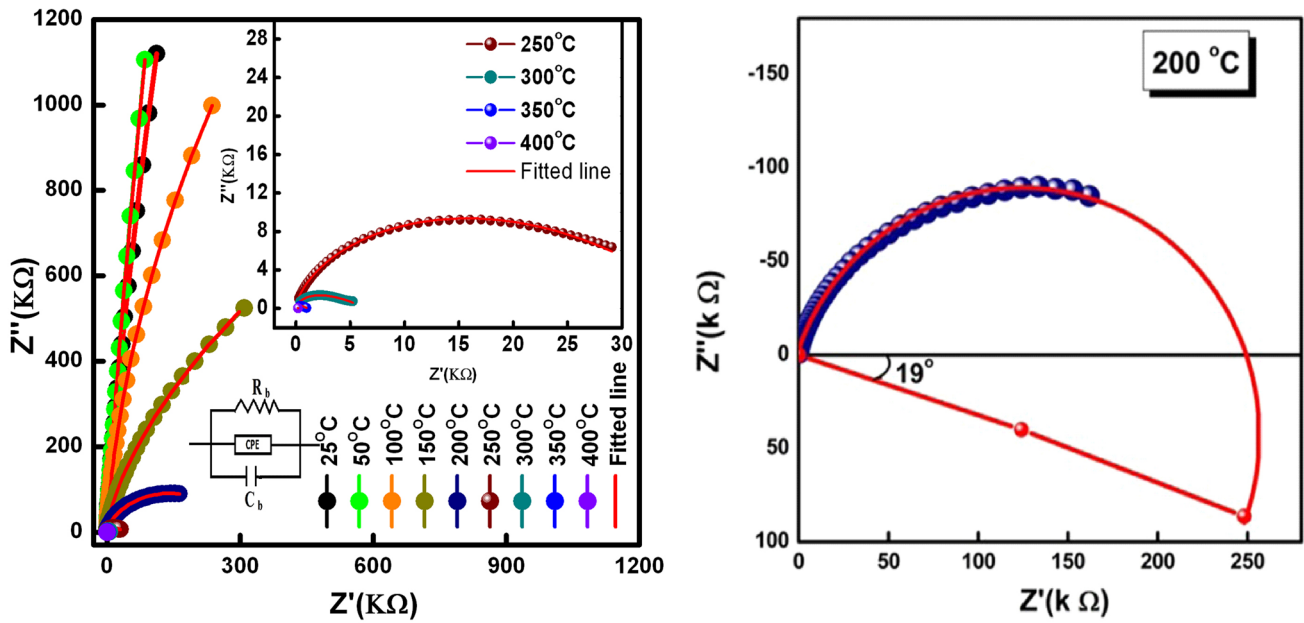


Fig. 5 Variation of Z'' with Z' of $\text{Bi}_{0.5}\text{Pb}_{0.5}\text{Fe}_{0.5}\text{Ce}_{0.5}\text{O}_3$ at different temperatures with angle of depression at 200 °C

admittance is generally represented as $Y(\text{CPE}) = A_0(j\omega)^n = A\omega^n + jB\omega^n$, [18] where $A = A_0\cos(n\pi/2)$ and $B = A_0\sin(n\pi/2)$. A_0 and n are frequency independent but temperature dependent parameters, A_0 determines the magnitude of the dispersion. The n varies between zero and one ($0 \leq n \leq 1$). The CPE describes an ideal capacitor for $n = 1$ and an ideal resistor for $n = 0$ [19–21]. In the present work, a single depressed semicircular arc was observed for all the studied temperatures. The single arc can be explained by an RQC network which suggests the grain contribution only. The value of resistance and capacitance of grains, exponent n and Q of $\text{Bi}_{0.5}\text{Pb}_{0.5}\text{Fe}_{0.5}\text{Ce}_{0.5}\text{O}_3$ is compared in Table 1. It was observed from the plot that the diameter of the arc (grain resistance) decreases with increasing temperature suggesting the NTCR behaviour. The non-Debye type behaviour was confirmed from the figure which shows the depression angle of 19° and the centre below the real Z axis at 200 °C.

Table 1 Comparison of resistance and capacitance of grains, exponent n and Q of $\text{Bi}_{0.5}\text{Pb}_{0.5}\text{Fe}_{0.5}\text{Ce}_{0.5}\text{O}_3$

Temperature (in °C)	R_g (in $\Omega \text{ cm}^2$)	C_g (farad/ cm^2)	n	CPE (Q)
25	9.666E10	1.159E–10	0.67	5.028E–10
50	5.554E12	1.119E–10	0.78	2.182E–10
100	7.013E6	1.133E–10	0.79	2.606E–10
150	5.906E6	1.23E–10	0.50	1.163E–8
200	3.151E5	1.17E–10	0.55	1.897E–8
250	3.701E4	1.216E–10	0.49	1.17E–7
300	6289	1.374E–10	0.39	1.201E–6
350	1050	1.274E–10	0.40	2.066E–6
400	226.9	4.154E–11	0.43	2.429E–6

3.4 Electrical conductivity

Figure 6a shows the plot of frequency-dependent AC conductivity (σ_{AC}) at some selected temperatures. Some dielectric data are used to calculate AC conductivity using an empirical relation:

$$\sigma_{AC} = \omega \epsilon_r \epsilon_0 \tan \delta \tag{1}$$

where ω is the angular frequency, ϵ_r is the relative dielectric constant, ϵ_0 is the permittivity of free space, and $\tan \delta$ is the tangent loss. The activation energy (E_a) at different temperature for both low- and high-frequency plot is calculated from the graph using the relation

$$\sigma = \sigma_0 \exp(-E_a/K_B T) \tag{2}$$

where σ_0 is the pre-exponential factor and K_B is the Boltzmann constant. The calculated value of E_a at frequencies from 1 kHz to 1 MHz at low temperatures (from

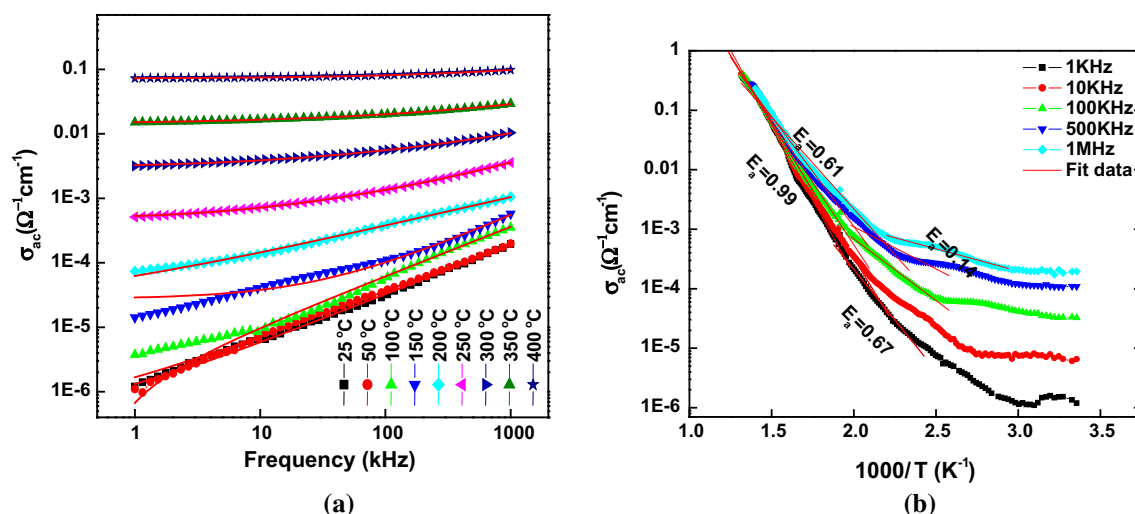


Fig. 6 Variation of AC conductivity (σ_{ac}) with **a** frequency at selected temperature and **b** inverse of absolute temperature at some selected frequency of $\text{Bi}_{0.5}\text{Pb}_{0.5}\text{Fe}_{0.5}\text{Ce}_{0.5}\text{O}_3$

30 to 200 °C) is 0.99, 0.90, 0.83, 0.73, and 0.61 eV. From temperature 200 to 450 °C, the E_a value is 0.67, 0.40, 0.40, 0.28, 0.14 eV. The high value of activation energy (>0.2 eV) suggests that the conduction mechanism is due to hopping [20]. It is observed that the value of σ_{AC} increases with increase in frequency in the low-temperature region, and becomes independent of frequency above certain high temperature. The frequency, at which AC conductivity dispersion takes place, is known as hopping frequency. As shown in the figure, it is found to increase on increasing temperature. Electrical conductivity consists of two parts; the frequency independent part, considered as dc conductivity, and the highly dispersive part considered as ac conductivity. According to Jonscher's power law [17], total conductivity can be expressed as

$$\sigma_t = \sigma_{dc} + B\omega^n \quad (3)$$

where, σ_t is the total conductivity, σ_{dc} the dc conductivity, $\sigma(\omega)$ is the ac conductivity at the angular frequency ω . B is a constant which depend on the intrinsic material property and temperature.

Figure 6b shows the variation of AC conductivity (σ_{ac}) of $\text{Bi}_{0.5}\text{Pb}_{0.5}\text{Fe}_{0.5}\text{Ce}_{0.5}\text{O}_3$ with inverse of absolute temperature ($10^3/T$) at different frequencies. As shown in the figure, the value of σ_{ac} increases with increase in temperature. This increase in conductivity at high temperatures can be explained by considering the mobility of charge carriers responsible for hopping, which also increases by increasing temperature. This situation suggests semiconducting behaviour of $\text{Bi}_{0.5}\text{Pb}_{0.5}\text{Fe}_{0.5}\text{Ce}_{0.5}\text{O}_3$ (BPFÇO). The activation energy at high frequency is found to be lower than that of the low-frequency region. This is due to the fact that at low frequencies the conductivity is taken by

mobility or transportation over long distances rather than by relaxation/orientation mechanism. The energy required for relaxation/orientation process is bigger than that required for mobility of charge carriers over longer distances [22, 23]. The value of activation energy obtained at higher temperatures is attributed to thermal motion of the oxygen vacancies or the formation of association among the oxygen vacancies and residual cations in the grain boundary [24, 25].

3.5 Electrical modulus analysis

The electrical modulus analysis is very useful to detect electrode polarization, grain boundary, conduction effect, bulk properties, electrical conductivity and relaxation time [26, 27]. This technique also provides an insight into the electrical processes occurring in the materials at different temperatures and frequencies. The following relations of electrical modulus can be used to estimate M' and M''

$$M' = A \left[\frac{(\omega RC)^2}{1 + (\omega RC)^2} \right] = A \left[\frac{\omega^2 \tau^2}{1 + \omega^2 \tau^2} \right]$$

$$M'' = A \left[\frac{\omega RC}{1 + (\omega RC)^2} \right] = A \left[\frac{\omega \tau}{1 + \omega^2 \tau^2} \right]$$

$$A = \frac{C_0}{C}$$

Using the above formalism, the inhomogeneous nature of polycrystalline sample with bulk and grain boundary effects can easily be probed which cannot be distinguished from complex impedance plots. The other major advantage of the electric modulus formalism is to suppress the electrode effect.

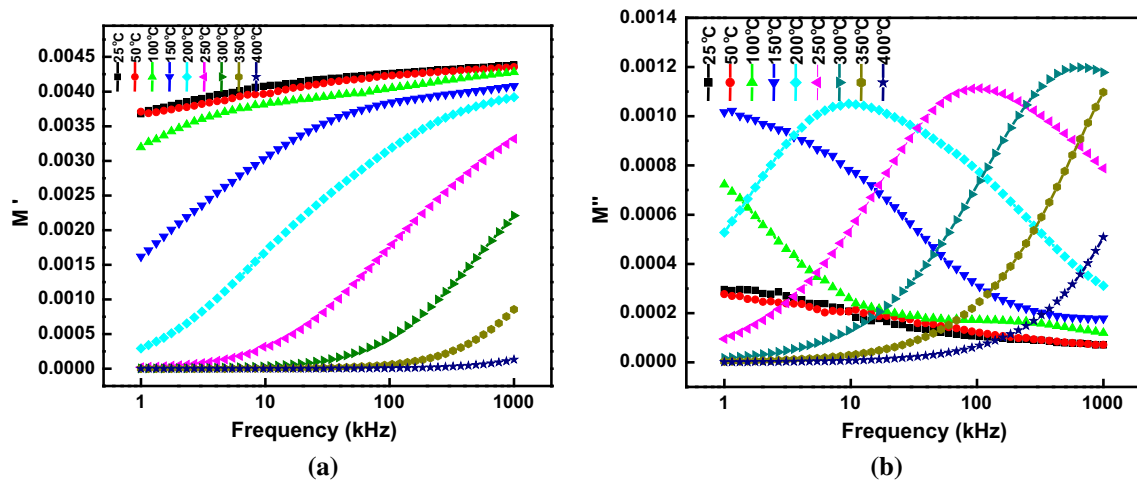


Fig. 7 Variation of M' (a) and M'' (b) with frequency at different temperatures of $\text{Bi}_{0.5}\text{Pb}_{0.5}\text{Fe}_{0.5}\text{Ce}_{0.5}\text{O}_3$

Figure 7a, b shows the variation of M' and M'' with frequency at a wide range of temperatures (25–400 °C). At low frequency, the value of M' tends to zero and the entire M' curve approaches to coincide at higher temperature. This may be due to presence of conduction phenomenon and short range mobility of charge carriers. This implies that there is a lack of restoring force for flow of charges under the influence of steady electric field [28]. But in our plot, the M' curve increases and are not reached to the high frequency where they have to coincide. It was observed (Fig. 7b) that with rise in temperature, the peak position (M''_{max}) shifts towards higher frequency. The shifting of the peak position indicates the thermally activated relaxation process in the material. In this relaxation process, generally the hopping mechanism of the charge carriers dominates. The broadening of the peaks was not of symmetric nature indicating the distribution of relaxation time (not a single relaxation time) and non-Debye type behavior. Because of the Debye type behavior, a symmetric peak with single relaxation time (not a broader peak) was observed.

4 Magneto-electric study

Magneto-electric effect is the property that (in certain materials), a magnetic field induces an electric polarization and an electric field induces a magnetization [29]. When the canted ferromagnetism in the material induces electric polarization resulting in an interaction between electric and magnetic dipoles, ME effect is observed. In another word, the criteria for the occurrence of ME effect in a material is the existence of magnetic and electric ordering in the material. This effect has been reported both in single phase

as well as composite materials. In the single phase material, M-E coupling arises due to the interaction between the magnetic and ferroelectric sub lattices, but in the composite the coupling arises due to the interaction of piezoelectric and piezo-magnetic phases [28, 30]. The canted anti-ferromagnetism ordering in BPFCE induces improper ferroelectric polarization, and hence there should be coupling between them to observe the ME effect. In order to get proper ME output, it is necessary to pole the sample both electrically and magnetically so that dipole ordering takes place, and the sub lattices effectively interact to yield the polarization [31].

The coupling of ME effect is generally characterized by ME voltage coefficient α_E which can be defined as [32, 33]

$$\alpha_E = \frac{dE}{dH} = \frac{V}{h_o d} \tag{4}$$

where E is the induced electric field, H is the applied magnetic field, V is the ME voltage developed across the sample, h_o is the magnitude of the AC magnetic field and d is thickness of the sample. The ME coefficient has been measured by dynamic method involving simultaneous application of AC as well as DC magnetic field [34]. The voltage developed across the BPFCE sample was measured using a ME set up interfaced with lock-in-amplifier. In the present study, 15.37 Oe AC magnetic fields and 1 kHz frequency were applied along with a DC magnetic field of varying magnitude (–5–5kOe). The AC field was produced by a Helmholtz coil (N = 200 turns with a radius, r = 2.5 cm and coil resistance, R = 23.4 Ω), which was driven by an AC current generated by a function generator. The magnitude of the AC magnetic field (h_o) generated at the centre of the Helmholtz coil can be calculated from the expression:

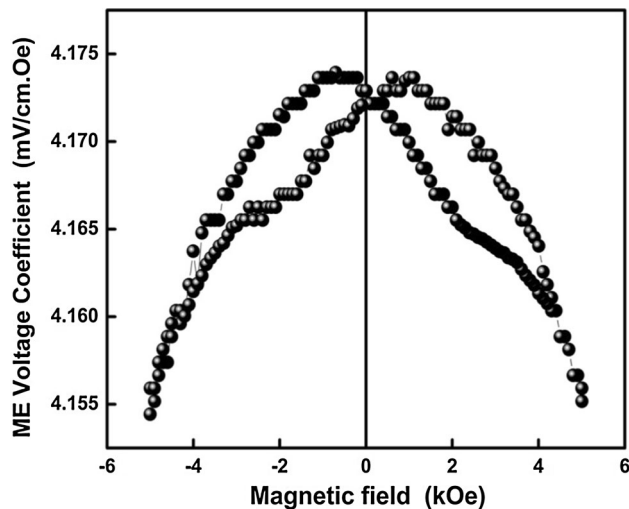


Fig. 8 Variation of ME voltage coefficient with applied DC magnetic field of $\text{Bi}_{0.5}\text{Pb}_{0.5}\text{Fe}_{0.5}\text{Ce}_{0.5}\text{O}_3$

$$h_o = \frac{\mu_0}{4\pi} \frac{2\pi N I r^2}{(r^2 + \frac{r^2}{4})^{\frac{3}{2}}} \times 2$$

$$= \frac{\mu_0}{(\frac{5}{4})^{\frac{3}{2}}} \frac{N I}{r} = 8.99 \times 10^{-3} \times \frac{N V}{r R} \text{ Oe}$$

Here, 5 V ac amplitude was applied to the Helmholtz coil resulting in a magnetic field of 15.37 Oe.

The variation of ME voltage coefficient with applied DC magnetic field of the BPFCE sample is shown in Fig. 8 for a longitudinal field arrangement. As reported earlier [35], the ME voltage developed across the sample due to the application of magnetic field can be written as:

$$E = V/d = f(H)$$

$$= \text{constant} + \alpha H + \beta H^2 + \gamma H^3 + \delta H^4 + \dots \quad (5)$$

$$\Rightarrow \frac{dE}{dH} = \alpha + 2\beta H + 3\gamma H^2 + 4\delta H^3 + \dots \quad (6)$$

The AC field (h) superimposed into the DC field (H) can be written as $h = h_o \sin \omega t$ and the total magnetic field can be expressed as: $H_{\text{total}} = H + h_o \sin \omega t$. The fourth order polynomial fitting of Fig. 8 gives the value of the entire coefficient. At zero magnetic fields, the ME voltage coefficient (α) was found to be 539×10^{-5} mV/cm.Oe. The second order co-efficient (β), third order co-efficient (γ) and the fourth order co-efficient (δ) were found to have values; 1.78×10^{-9} , 8.46×10^{-13} and 8.66×10^{-17} (in appropriate units) respectively.

5 Conclusions

In summary, $\text{Bi}_{0.5}\text{Pb}_{0.5}\text{Fe}_{0.5}\text{Ce}_{0.5}\text{O}_3$ powder was successfully synthesized by a high-temperature solid-state synthesis method. Preliminary X-ray structural analysis

confirms the monoclinic structure of the compound. The SEM micrograph shows that the elongated grains are uniformly distributed throughout the surface of the sample, and are in the range of 2–7 μm . The dielectric parameters of the compound or system are strongly dependent on temperature and frequency. Impedance spectra lead to conclude that the conduction contribution is due to both bulk material (up to 300 $^{\circ}\text{C}$) and grain boundary effect ($T > 350$ $^{\circ}\text{C}$). It also suggests that the dielectric relaxation in the material is of poly-dispersive non-Debye type. The frequency dependence of AC conductivity obeys Joncher's universal power law. The linear variation of the conductivity pattern is attributed to Arrhenius type thermally activated electrical transport phenomena. The ME coupling coefficients of different orders have provided useful information on the material developed.

Acknowledgments The authors are grateful to Dr. Raja Kishora Lenka of Powder Metallurgy Division, BARC, Mumbai, Dr. Rosalini Sahu (KIIT University), Ms. Sushrisangita Sahoo and Mrs. T. Acharya for their kind helps in some experiments and analysis work.

Compliance with ethical standards

Conflict of interest The authors declare that there is no conflict of interest.

References

- G.A. Smolenskii, I.E. Chupis, *Sov. Phys. Usp.* **25**, 475 (1982)
- A. Lahmar, S. Habouti, M. Dietze, C.H. Solterbeck, M. Es-Souni, *Appl. Phys. Lett.* **94**, 012903 (2009)
- J.A.M. Cagigas, D.S. Candela, E. Baggio-Saitovitch, *J. Phys.* **200**, 012134 (2010)
- S. Pattanayak, B.N. Parida, P.R. Das, R.N.P. Choudhary, *Appl. Phys. A* **112**, 387–395 (2013)
- C. Lan, Y. Jiang, S. Yang, *J. Mater. Sci.* **46**, 734738 (2011)
- G.S. Lotey, N.K. Verma, *J. Nanopart. Res.* **14**, 742 (2012)
- R. Mazumder, P.S. Devi, D. Bhattacharya, P. Choudhury, A. Sen, M. Raja, *Appl. Phys. Lett.* **91**, 062510 (2007)
- S. Pattanayak, R.N.P. Choudhary, D. Pattanayak, *J Mater Sci Mater Electron.* **25**, 3854–3861 (2014)
- J. Rout, R.N.P. Choudhary, H.B. Sharma, S.R. Shannigrahi, *Ceram. Int.* **41**(7), 9078–9087 (2015)
- S. Das, R. Padhee, P.R. Das, R.N.P. Choudhary, *Phase Transit* **87**(3), 223–235 (2014)
- E W POWD, An interactive powder diffraction data interpretation and indexing program, Ver. 2.1, School of physical science, Finders University of South Australia, Bedford Park, S.A. 5042, Australia
- D.C.L. Vasconcelos, V.C. Costa, E.H.M. Nunes, A.C.S. Sabioni, M. Gasparon, W.L. Vasconcelos, *Mater. Sci. Appl.* **2**, 1375–1382 (2011)
- C.G. Koop, *Phys. Rev.* **83**, 121–124 (1951)
- R.P. Pawar, V. Puri, *Ceram. Int.* **40**, 10423–10430 (2014)
- T. Acharya, R.N.P. Choudhary, *J. Electron. Mater.* **44**, 271–280 (2015)
- A. Kumar, B.P. Singh, R.N.P. Choudhary, A.K. Thakur, *J. Alloy. Compd.* **394**, 292–302 (2005)

17. M. Ram, J. Alloy. Compd. **509**, 1744–1748 (2011)
18. C.K. Suman, K. Prasad, R.N.P. Choudhary, J. Mater. Sci. **41**, 369 (2006)
19. A.K. Jonscher, Nature **267**, 673 (1977)
20. S. Sen, R.N.P. Choudhary, P. Pramanik, Phys. B **387**, 56 (2007)
21. R. Padhee, P.R. Das, B.N. Parida, R.N.P. Choudhary, J. Mater. Sci. Mater. Electron. (2012). doi:[10.1007/s10854-012-0647](https://doi.org/10.1007/s10854-012-0647)
22. M.A.E.F. Gabal, Y.M. Al Angari, A.Y. Obaid, C. R. Chim. **16**, 704–711 (2013)
23. N. Hirose, A.R. West, J. Am. Ceram. Soc. **79**, 1633 (1996)
24. A. Belboukhari, E. Choukri, Y. Gagou, R. Elmoznine, N. Abdelmoula, A. Neqali, M. El Marssi, H. Khemakhem, D. Mezzane, Superlattices. Microstruct. **71**, 7–22 (2014)
25. K.S. Rao, P.M. Krishna, D.M. Prasad, Physica Status Solidi (b) **244**, 2267 (2007)
26. A.R. James, K. Srinivas, Mater. Res. Bull. **34**, 1301 (1999)
27. I.M. Hodge, M.D. Ingram, A.R. West, J. Electroanal. Chem. **58**, 429 (1975)
28. R. Macdonald, Solid State Ionics **13**, 147 (1984)
29. Y. Zhanga, J.P. Zhou, Q. Liu, S. Zhang, C.Y. Deng, Ceram. Int. **40**, 5853 (2014)
30. D.C.L. Vasconcelos, V.C. Costa, E.H.M. Nunes, A.C.S. Sabioni, M. Gasparon, W.L. Vasconcelos, Mater. Sci. Appl. **2**, 1375–1382 (2011)
31. M.M. Kumar, A. Srinivas, S.V. Suryanarayana, G.S. Kumar, T. Bhimasankaram, An experimental setup for dynamic measurement of magnetoelectric effect. Bull. Mater. Sci. **21**, 251 (1998)
32. M. Shi, R. Zuo, Y. Xun, L. Wang, C. Gu, H. Su, J. Zhong, G. Yu Ceram. Int. **40**, 9249 (2014)
33. J.K. Dipti, S. Juneja, K.K. Singh, C. Raina, Prakash. Ceram. Int. **41**, 6108 (2015)
34. P. Pahuja, C. Prakash, R.P. Tandon, Ceram. Int. **40**, 5731 (2014)
35. G.V. Duonga, R. Groessinger, M. Schoenhardt, D. Bueno-Basques, J. Mag. Mag. Mater. **316**, 390 (2007)